20 Feb 2022

Design, Dynamic Performance and Ecological Efficiency of Fiber-Reinforced Mortars with Different Binder Systems: Ordinary Portland Cement, Limestone Calcined Clay Cement and Alkali-Activated Slag

Wu Jian Long

Zhuorui Wu

Kamal Khayat
Missouri University of Science and Technology, khayatk@mst.edu

Jingjie Wei

et. al. For a complete list of authors, see https://scholarsmine.mst.edu/civarc_enveng_facwork/2357

Recommended Citation

W. J. Long et al., "Design, Dynamic Performance and Ecological Efficiency of Fiber-Reinforced Mortars with Different Binder Systems: Ordinary Portland Cement, Limestone Calcined Clay Cement and Alkali-Activated Slag," *Journal of Cleaner Production*, vol. 337, article no. 130478, Elsevier, Feb 2022.
The definitive version is available at https://doi.org/10.1016/j.jclepro.2022.130478

Journal of Cleaner Production 337 (2022) 130478

Contents lists available at ScienceDirect

Journal of Cleaner Production

journal homepage: www.elsevier.com/locate/jclepro

Design, dynamic performance and ecological efficiency of fiber-reinforced mortars with different binder systems: Ordinary Portland cement, limestone calcined clay cement and alkali-activated slag

Wu-Jian Long [a], Zhuorui Wu [a,c], Kamal H. Khayat [b], Jingjie Wei [a,b,*], Biqin Dong [a], Feng Xing [a], Jinrui Zhang [d]

[a] Guangdong Provincial Key Laboratory of Durability for Marine Civil Engineering, Key Lab of Coastal Urban Resilient Infrastructure, MOE, College of Civil and Transportation Engineering, Shenzhen University, Shenzhen, 518060, Guangdong, PR China
[b] Department of Civil, Architectural and Environmental Engineering, Center for Infrastructure Engineering Studies, Missouri University of Science and Technology, Rolla, MO, 65401, USA
[c] Sino-Australia Joint Research Center in BIM and Smart Construction, Shenzhen University, Shenzhen, 518060, Guangdong, PR China
[d] State Key Laboratory of Hydraulic Engineering Simulation and Safety, Tianjin University, Tianjin, 300072, PR China

ARTICLE INFO

Handling Editor: Zhen Leng

Keywords:
Dynamic mechanical property
Fiber-reinforced mortar
Limestone calcined clay cement
Alkali-activated slag
Microstructure
Ecological evaluation

ABSTRACT

The dynamic mechanical properties and ecological efficiency of cement-based composites are of vital importance to the development of green building materials and dynamic loadings resistance. In this study, the dynamic mechanical properties, ecological and economic efficiency of fiber-reinforced mortars (FRMs) made with different binder systems, including ordinary Portland cement (OPC), limestone calcined clay cement (LC^3), and alkali-activated slag (AAS), were compared. In addition, different rheological parameters were designed to evaluate the dynamic mechanical properties of FRMs. The fiber pull-out testing, Barrett-Joyner-Halenda (BJH) testing, and scanning electron microscope (SEM) were used to reveal the difference in the dynamic mechanical properties of FRMs made with different binder systems. The results showed that the loss factor of FRM made with LC^3 was the highest, 70% and 150% higher than that made with OPC and AAS as the plastic viscosity of mixtures was at the same range. In addition, the loss factor of FRMs made with OPC and LC^3 improved by 25% and 8.6% respectively as the plastic viscosity was improved to a higher level and caused more uniform fiber distribution. The fiber pull-out and microstructure testing indicated that FRM made with LC^3 showed appropriate pore size distributions and good fiber-matrix interfacial properties. The ecological evaluation and cost analysis showed that the EE, ECO_2e, and the cost of unit loss factor of FRM made with LC^3 were the lowest among three kinds of mortars, showing 48369.1 MJ/m^3, 6894.4 $kgCO_2/m^3$, and 20288.0 RMB/m^3 respectively. Compared with FRM made with OPC, the above parameters were reduced by 55.8%, 66.9% and 46.0% respectively. Therefore, the FRM made with LC^3 shows higher potential for designing green building materials with great dynamic loadings resistance, compared with FRMs made with OPC and AAS.

1. Introduction

Currently, the human society is faced with serious environmental degradation. With an unprecedented growth of human population and industrialization revolution, a large amount of CO_2 is emitted and causes serious climate warming. According to a report from the University of Oxford (Pierrehumbert, 2019), the global carbon emissions will reach 2 trillion tons in 50 years, leading to 4 °C of warming. As early as 2012, the World Bank actually announced that 4 °C of global warming would be "cataclysmic" (World-Bank, 2012). Climate warming has led to a series of risks, such as sea levels rise, loss of coastal areas, and occurrence of natural disasters (Benhelal et al., 2013), which attracted extensive attention.

Concrete has become the most widespread building material in the world over the past few decades due to its excellent mechanical performance, durability, and low cost (Liew et al., 2017; Zamora-Castro et al., 2021). However, the use of concrete has aroused worldwide concerns due to the excessive consumption of natural resources and the

* Corresponding author. College of Civil and Transportation Engineering, Shenzhen University, Shenzhen, 518060, Guangdong, PR China.
E-mail addresses: jwxhc@mst.edu, Weijj@szu.edu.cn (J. Wei).

https://doi.org/10.1016/j.jclepro.2022.130478
Received 30 July 2021; Received in revised form 12 December 2021; Accepted 9 January 2022
Available online 12 January 2022

CO_2 emissions in cement manufacturing (Gupta et al., 2021). At present, the cement production in the world has risen to 4.0 Gt per year (Kaliyavaradhan and Ling, 2017). It is reported that 0.85 tons of CO_2 will be emitted per ton of cement produced (Ostovari et al., 2021), and cement alone accounts for 5–7% of CO_2 anthropogenic global emissions and 3% of global greenhouse gas emissions (Van den Heede and De Belie, 2012). Therefore, to reduce the environmental problems caused by cement, there is an urgent need for cement substitutes.

Mineral admixtures, also known as supplementary cementitious materials (SCMs), are considered to have the potential to reduce the environmental pollution caused by the cement industry. In addition, the filling effect and high pozzolanic activities of SCMs can significantly improve the performances of concrete (Ashish, 2019; Liu and Wang, 2017; Siddique et al., 2021). For example, slag, one of the most common industry wastes, is usually added into concrete as SCMs to replace part of cement, which greatly improves the mechanical properties and durability of concrete and benefits environmental protection (Ayub et al., 2014; Liu et al., 2014). However, when the cement replacement rate reaches a certain level, the effect of slag may be the opposite (Aghaeipour and Madhkhan, 2017; Lee et al., 2015), which limits the environmental benefits of slag. Alkali-activated slag (AAS) cementitious materials, composed of alkaline activators and slag, solve this problem. Compared with cement-based composites with SCMs, the AAS-based composites which completely replace cement with slag can still maintain satisfactory performances, including excellent early mechanical properties, durability, and low carbon emissions (Amran et al., 2021; Mohamed, 2019). As a result, AAS-based composites are recognized as a potential alternative to conventional cement-based composites. However, AAS has some defects such as large shrinkage and easy cracking (Li et al., 2021; Mastali et al., 2018). In addition, the amount of slag available in the world is only 10% of cement production (Scrivener et al., 2018), which limits the further application of AAS in construction engineering. Limestone calcined clay cement (LC^3) is also a new type of sustainable cementitious material, which can reduce CO_2 emissions by 30% compared with OPC (Sanchez Berriel et al., 2016). LC^3 consists of ground clinker, calcined clay, limestone, and gypsum. The high pozzolanic activity of calcined clay and the filling effect of limestone powder significantly enhanced the mechanical properties and durability of LC^3-based composites (Dhandapani et al., 2018). In addition, calcined clay is obtained by calcining clay which is widely distributed in the world and rich in reserves, while the amount of slag available is limited (Scrivener et al., 2018). Thus, compared with slag, LC^3 is considered to have more potential in replacing traditional cement materials.

In addition to environmental pollution, it's difficult for ordinary cement-based composites to reduce the vibrations to the specified low value, that is, the particle peak vibration is less than 50 mm/s. This results in poor dynamic mechanical properties (Kim et al., 2014; Ou et al., 2008). The dynamic mechanical properties are an important performance index of cement-based composites, which are closely related to the structural dynamic response, materials damage, and damping energy consumption (Luo et al., 2015; Pham et al., 2015; Zhang et al., 2020). For traditional concrete structures, when subjected to dynamic loads such as winds, sounds, or even earthquakes, are easy to be damaged and cause huge economic losses. In the United States, earthquakes cause $6.1 billion in building damage each year, according to the FEMA (Federal Emergency Management Agency) (Jaiswal et al., 2017). If the dynamic mechanical properties of materials reach a certain level, the cooperation of materials and structures will bring enough capacity to dissipate the vibrating energy, which will greatly reduce the cost caused by structural damage under dynamic loads (Khan et al., 2021; Long et al., 2017b; Xue and Shinozuka, 2013).

Recently, damped materials such as fiber (Huang et al., 2020), rubber (Dehdezi et al., 2015), and polymer latex (Pan et al., 2012) have been proved to be effective in improving the dynamic mechanical properties of cement-based composites, among which fiber is considered the most popular additives. The fiber supports part of the stress by bridging cracks in the matrix and improves the toughness, ductility, and energy consumption of cement-based composites. Zhao et al. (2020) found that when the volume fraction of steel fibers was 1.5%, the dynamic splitting strength and energy dissipation of ultra-high toughness cementitious composites increased by 7–29% and 2.5–41%, respectively. Wang and Wang (2013) studied the impact resistance of lightweight aggregate concrete and found that the addition of steel fiber with a 1.5% volume fraction effectively increased the first-crack and failure strength of lightweight aggregate concrete by 4 folds and 8.5 folds. Zhang et al. (2020) found that the impact strength of concrete can be enhanced by both basalt fiber and macro synthetic polypropylene fiber. When the fiber hybrid ratio was 0.075%~0.35%, the concrete achieved the best impact resistance.

Many studies have been carried out on fiber-reinforced AAS-based composites and fiber-reinforced LC^3-based composites. However, most of these studies are limited to the basic properties (such as workability, static mechanical properties, and durability) of the above two kinds of fiber-reinforced composites (Behfarnia and Rostami, 2017; Dhandapani et al., 2018; Farhan et al., 2018; Wang et al., 2021), and few studies investigate the difference in dynamic mechanical properties between the two kinds of fiber-reinforced composites. In addition, the effect of rheological parameter on the dynamic mechanical properties of fiber-reinforced composites is also not clear.

This study aims to realize the cleaner production of fiber-reinforced mortars with good dynamic loadings resistance. Specifically, the dynamic mechanical properties of fiber-reinforced mortars (FRMs) made with different binder systems (OPC, LC^3, and AAS) and different fiber distribution obtained by adjusting the rheological parameter of mixtures were compared in this study. In addition, the ecological and economic efficiency of the three kinds of mortars were also evaluated. Finally, one kind of FRM with better dynamic mechanical properties, environmental protection, and lower cost was recommended for designing cleaner product of fiber-reinforced mortars with good dynamic loadings resistance. Polycarboxylate-based high-range water-reducing admixture (HRWRA) and hydroxypropyl methylcellulose (HPMC) were used to adjust the rheological parameter of mixtures so as to study the effect of fiber distribution on the dynamic mechanical properties of mortars. In addition, the fiber-matrix interfacial bond properties and the pore structure of mortars were also investigated to reveal the difference in the dynamic mechanical properties of FRMs made with different binder systems.

2. Materials and methods

2.1. Materials

Ordinary Portland cement (PO 42.5R) conforming to the Chinese standard (GB/T175, 2007) was used in this study. To achieve the cleaner production of mortars, the S95 ground granulated blast-furnace slag and LC^3 were also used, among which the S95 ground granulated blast-furnace slag was conforming to the Chinese standard (GB/T18046, 2017), and the LC^3 was provided by Sinoma International Engineering Co., LTD., consisting of ground clinker, calcined clay, limestone, and gypsum. The chemical compositions of raw materials used in this study were tested by X-ray fluorescence spectrometer (SPECTRO iQ, provided by SPECTRO Analytical Instruments, Germany), and the results were shown in Table 1. In addition, the particle size distribution of raw materials is shown in Fig. 1. River sand conforming to the Chinese standard (GB/T14684, 2011) was provided by Xiamen ISO Standard Sand CO., LTD. The physical properties of the river sand are given in Table 2, provided by the manufacture. Straight steel fibers with a diameter of 0.2 mm and a length of 13 mm were used in this study. The tensile strength and the elastic modulus of straight steel fiber were 2.0 GPa and 203 GPa, respectively.

Analytically pure sodium hydroxide particles (NaOH, 96% purity) and liquid sodium silicate (LSS, containing 8.9 wt% Na_2O, 28.8 wt%

Table 1
Chemical compositions of various raw materials (mass %).

Material	CaO	SiO_2	Al_2O_3	Fe_2O_3	MgO	SO_3	K_2O	Na_2O	LOI
cement	64.45	20.59	5.62	3.78	2.11	2.1	0.28	0.2	0.87
ground clinker	63.17	23.18	4.52	4.65	2.31	0.59	0.23	0.46	0.89
calcined clay	0.34	64.19	28.5	0.62	0.16	-	0.26	0.11	5.82
limestone	46.17	12.49	3.64	2.53	1.98	-	0.6	0.61	31.98
gypsum	35.71	4.75	0.64	0.61	1.45	39.76	0.04	0.04	17
slag	38.89	36.21	15.28	0.2	7.36	-	0.38	0.91	0.77

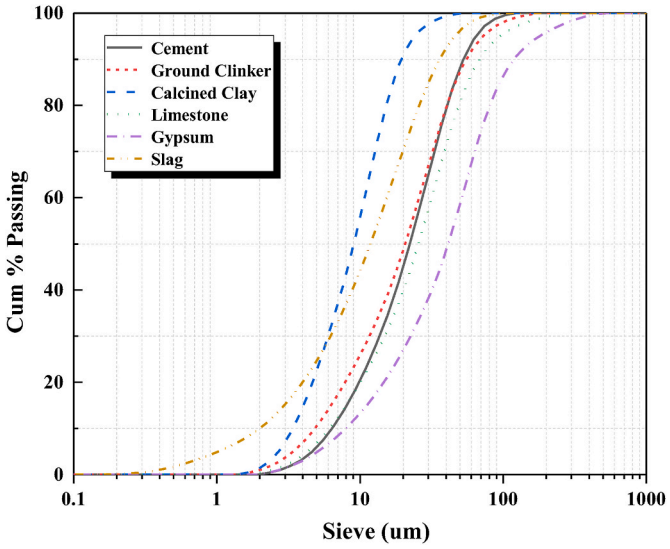

Fig. 1. Particle size distribution of various raw materials.

Table 2
Physical properties of the river sand.

	River sand
Roundness	0.5
Apparent density (g/cm^3)	2.63
Mass density (g/cm^3)	1.49
Compact density (g/cm^3)	1.58
Water absorption (%)	0.55
Shear modulus (MPa)	1
Coefficient of uniformity	1.62

SiO_2, and 62.3 wt% H_2O) were used to prepare alkaline activators. Polycarboxylate-based high-range water-reducing admixture (HRWRA, maximum water reduction levels ranged between 35% and 39%) and hydroxypropyl methylcellulose (HPMC, specific gravity ranged between 1.26 and 1.31) were used to control the rheological properties of mixtures.

2.2. Mix proportions

As shown in Table 3, three types of cementitious materials including OPC, LC^3, and AAS were employed to design the mixtures in this study. LC^3 consisted of ground clinker, calcined clay, limestone, and gypsum with a mass ratio of 5:4:0.5:0.5. To ensure the workability of mixtures, the mass ratios of water to binder (W/B) and sand to binder were set to 0.45 and 1.5, respectively. In addition, the mixtures had 1% (vol.) steel fibers. According to previous studies (Jasiuniene et al., 2018; Kang et al., 2019; Meng and Khayat, 2017; Teng et al., 2020; Wang et al., 2017), there is a corresponding relationship between fiber distribution and the rheological properties of mixtures, and if the same procedure is used to cast all samples, the fiber distribution of samples could be ensured in the same range when the fresh mortars show the same rheological properties. To eliminate the interference of fiber distribution when comparing the dynamic mechanical properties of FRMs made with different binder systems, the rheological parameters of the three kinds of mixtures were adjusted to be consistent, so as to ensure the fiber distribution at the same range. As mentioned earlier, the rheological parameters of mixtures were adjusted by the synergistic action of HRWRA and HPMC. To obtain the target rheological parameters, repeated tests were need to determine the contents of HRWRA and HPMC. Due to the insensitivity of alkali-activated slag cementitious materials to HRWRA, the yield stress and viscosity of alkali-activated slag mortar (AASM) were taken as the benchmark in the rheological control in this study. To make the rheological parameters of FRMs made with OPC and LC^3 consistent with AASM, the following two steps are required:

1) Adjust the yield stress of FRMs made with OPC and LC^3 to be consistent with AASM and the mixtures were named OPC-1 and LC^3-1. Only HRWRA was introduced in this step, which mainly used to reduce the yield stress of mixtures. In addition, the HRWRA contents of LC^3-1 was significantly higher than that of OPC-1. This was due to the smaller particle fineness of calcined clay which resulted in stronger water absorption. This result was consistent with the findings of Dhandapani et al. (2018).
2) Adjust the viscosity of FRMs made with OPC and LC^3 to be consistent with AASM after obtaining the same yield stress in three mixtures, and the mixtures were named OPC-2 and LC^3-2. Both HRWRA and HPMC were introduced in this step, among which HPMC was mainly used to increase the viscosity of mixtures. In addition, more HRWRA was used to maintain the yield stress, which also slightly increased due to the use of HPMC.

The fiber distribution of FRMs made with OPC and LC^3 in these two steps would be different (Teng et al., 2020; Wang et al., 2017), so as to analyze the effect of fiber distribution on dynamic mechanical properties.

The mixing procedure of all mixtures was illustrated in Fig. 2. To

Table 3
Mix proportions of the mortars used in this study (in g unless otherwise noted).

Mix ID	Cement	LC^3	Slag	Sand	SF	W/B	Water	NaOH	LSS	HPMC	HRWRA
OPC-1	840	-	-	1260	83.3	0.45	378	-	-	-	1.64
OPC-2	840	-	-	1260	83.3	0.45	378	-	-	1.01	10.08
LC^3-1	-	840	-	1260	83.3	0.45	378	-	-	-	7.81
LC^3-2	-	840	-	1260	83.3	0.45	378	-	-	0.42	12.6
AASM	-		840	1260	83.3	0.45	314.68	24.33	101.64	-	-

SF: steel fiber; LSS: liquid sodium silicate; HPMC: hydroxypropyl methyl cellulose; HRWRA: high-range water-reducing admixture.

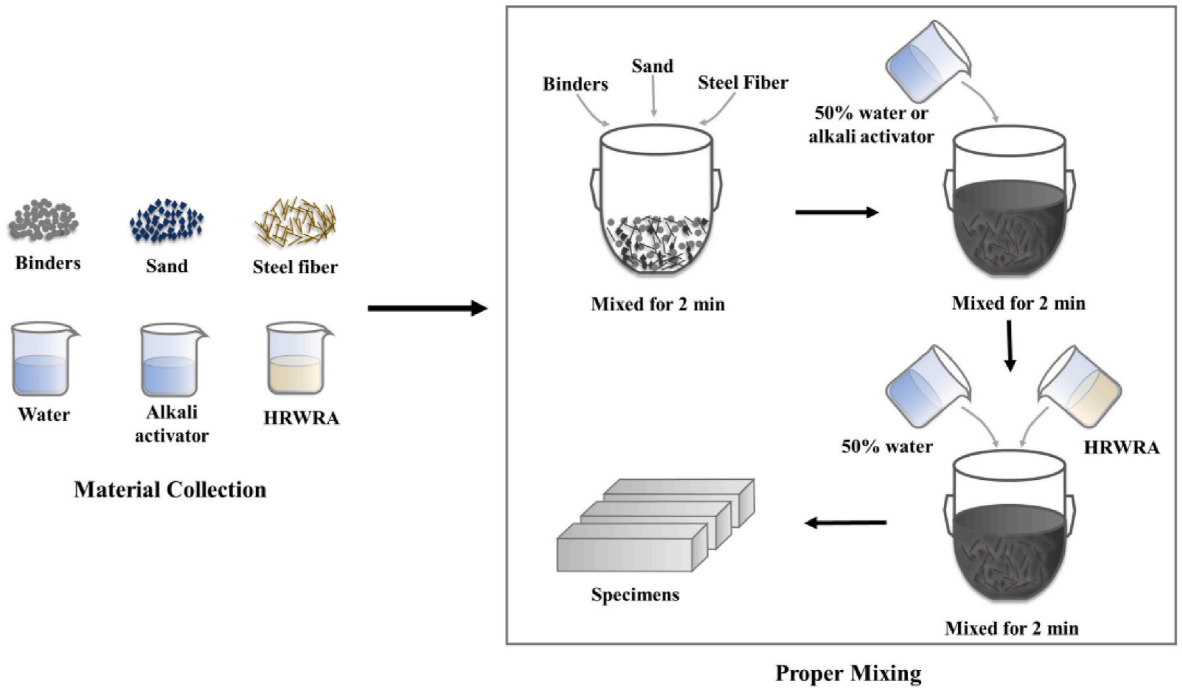

Fig. 2. The mixing procedure for mortars.

prepare the activator solution, NaOH was dissolved in water and then mixed with LSS to adjust the modulus (molar ratio of SiO_2 to Na_2O) of the activator solution to be 1.2. The mixing procedure of mixtures was as follows: 1) dry components, including binders, sand, and fibers were mixed at a low speed for 2 min; 2) 50% of the mixing water or the premixed activator solution for AASM was added and mixed at a low speed for 2 min; 3) Finally, the remaining mixing water and HRWRA was slowly added, followed by high-speed mixing for 2 min. In total, 6 min was required for mixing. The obtained mixtures were then cast into steel molds with dimensions of 40 × 40 × 160 mm^3 and dog-bone-shaped molds. The specimens were covered with a plastic sheet for one day, then de-molded and stored in a standard curing room with a relative humidity ≥95% and a temperature of 20 ± 3 °C until testing.

2.3. Test methods

2.3.1. Fresh properties

The mini-slump test was conducted based on the Chinese standard (GB/T2419, 2005). The mixtures were filled into a mini-slump cone with 60 mm height, 70 mm top opening and 100 mm bottom opening. Then, the mini-slump cone was lifted vertically to allow the mixtures to flow liberally. The diameter of mixtures was measured in two directions perpendicular to each other after the mixture stop flowing. The average value was defined as the slump flow of mixtures.

In this study, two rheological parameters of mixtures including yield stress (τ_0) and plastic viscosity (μ) were measured by the RM 100 PLUS rheometer (Lamy Rheology Instruments Company, Champagne-au-Mont-d'Or, France), and the measuring system was MS-R3. Note that the yield stress mentioned in this study refers to the minimum stress that maintains the flow of mixtures, also known as dynamic yield stress (Qian and Kawashima, 2018). The working principle of the rheometer is to convert the rotational velocity and torque collected during the rheological test into shear stress (τ) and shear rate (γ), and the yield stress and plastic viscosity of mixtures can be measured from the flow curve that obtained by fitting the relationship between τ and γ. This involves two aspects: one is the method to measure the yield stress and plastic viscosity from the flow curve, and the other is the selection of fitting model. Generally, the yield stress is obtained by extending the flow curve and is determined as the shear stress at zero shear rate, while the plastic viscosity is determined as the slope of flow curve (Rubio-Hernandez et al., 2020). In addition, the flow curves of cement-based materials can be well fitted by Bingham model represented by Eq. (1), according to previous studies(Meng and Khayat, 2017; Teng et al., 2020). Bingham model is the most commonly used rheology model for cement-based materials. For most fresh cement-based materials, Bingham model can well meet the requirements of rheological measurement in engineering, and its calculation is simple and convenient.

$$\tau = \tau_0 + \mu\gamma \tag{1}$$

where τ_0 represents the yield stress, μ represents the plastic viscosity, τ and γ represent the shear stress and shear rate.

The test procedure of the rheology test is illustrated in Fig. 3. To guarantee the uniformity of measurement results, the mixtures were pre-

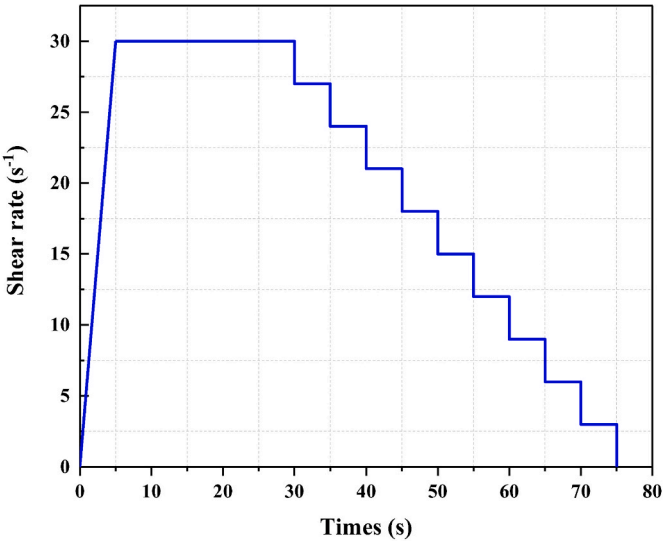

Fig. 3. Procedure of rheology test.

shared at a speed of 30 s^{-1} for 25s. Then, the mixtures were sheared in continuous velocity decreased from 30s^{-1} to 0 for 50s. Finally, the yield stress and plastic viscosity of mixtures were calculated according to the relationship between shear stress and shear rate obtained from the rheology test, based on the Bingham model represented by Eq. (1). In this study, all data points (shear stress and shear rate) were determined by the average value of three test results, data points that deviated from the fitting line by more than 10% would be eliminated.

2.3.2. Evaluation of fiber distribution

To evaluate the fiber distribution of mortars, specimens with dimensions of 40 × 40 × 160 mm^3 were cut from the middle along the direction of the cross-section. Then, the surfaces of segmented specimens were sequentially polished by silicon carbide papers with grit sizes of 200, 400, and 600 and imaged by a professional digital camera in a micro-studio. After that, the images were further converted to binary images, and the fiber distribution was quantitatively evaluated using ImageJ (an image analysis tool). In the binary image, the steel fibers were usually shown as white dots, while the mortar matrix was shown as a black background (see Section 3.2). Therefore, the image analysis tool could evaluate the distribution of fibers in the matrix by analyzing the distribution of white dots in the black background. To evaluate the distribution of white dots, the binary image should be divided into a certain number of rectangular units, and then the uniformity of the number distribution of white dots in each unit would be evaluated through a quantitative index.

According to the previous studies (Alberti et al., 2016; Song et al., 2018), the total cross-sectional area of 40 × 40 mm^2 was divided into 3 × 3 units for fiber distribution analysis. Fiber distribution coefficient (α) was used to quantitatively evaluate the fiber distribution of the cross-section (Teng et al., 2020), as shown in Eq. (2):

$$\alpha = \exp\left[-\frac{1}{x_0}\sqrt{\frac{\sum(x_i - x_0)^2}{n}}\right] \quad (2)$$

where n is the number of the units, x_i represents the number of white dots in the i-th unit, x_0 represents the average number of white dots in each unit.

2.3.3. Static mechanical properties

According to the Chinese Standard (GB/T17671, 1999), the mechanical properties of all mixtures were tested at 28d. The flexural strength of specimens with dimensions of 40 × 40 × 160 mm^3 was first tested by the third-point bending test, and then the specimens obtained from the flexural test were used to test the compressive strength. The flexural and compressive strengths of each group were determined by the average value of three specimens.

2.3.4. Fiber pull-out testing

The dog-bone-shaped specimen used for fiber pull-out testing and the test apparatus is shown in Fig. 4. According to Chinese standard (CECS13, 2009), a piece of thin plastic sheet with a smooth surface was used to avoid adhesion and divide the specimen into two halves, namely, the pull-out half and the fixed half (Pi et al., 2019). Four steel fibers with a length of 13 mm were vertically fixed on the plastic sheet by using glue. To ensure that the fibers were all pulled out from the pull-out half, the embedment length of fibers in the pull-out half and the fixed half was set to 5 mm and 8 mm, respectively. Then, the plastic sheet was inserted into the middle of the mold. The specimens were demolded 24 h after casting and cured in a standard curing room for 28d.

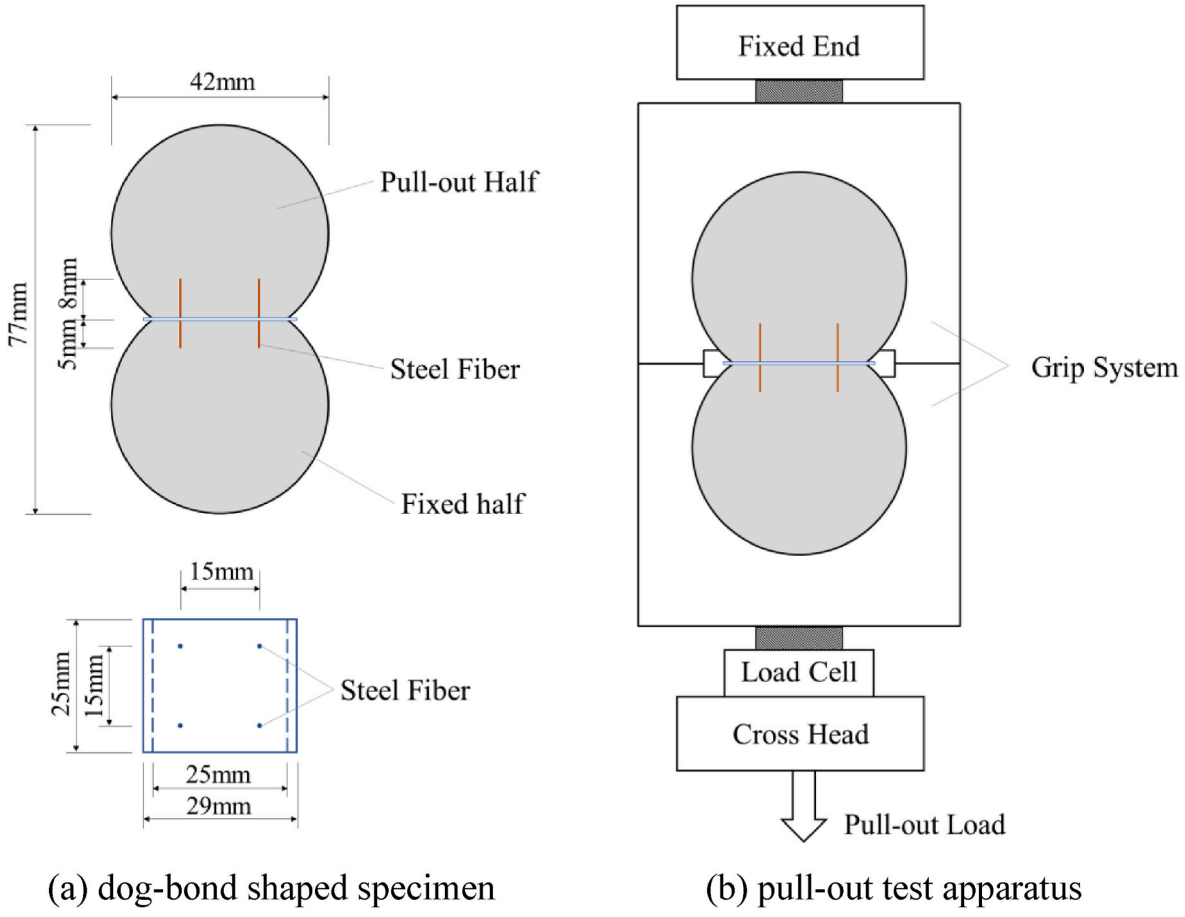

Fig. 4. Illustration of dog-bond shaped specimen pull-out test apparatus.

In this study, an electronic universal testing machine with a 10 kN load cell (provided by Jinan Docer Testing Machine Technology Co., Ltd) was used for fiber pull-out testing under a loading rate of 1 mm/min. To ensure the reliability of the pull-out load-slip relationship recorded, six specimens were tested for each mixture. The bond strength can be calculated as Eq. (3):

$$\tau_{max} = \frac{P_{max}}{n\pi dl} \tag{3}$$

where τ_{max} (Mpa) is the bond strength of embedded fiber; P_{max} (N) is the maximum pull-out load; d (mm) is the diameter of a single fiber (0.2 mm); l (mm) is the embedment length of the fiber in the pull-out half (5 mm); n is the number of fiber embedded in a dog-bone specimen.

2.3.5. Dynamic mechanical analysis (DMA)

As shown in Fig. 5, a dynamic mechanical analyzer (DMA+ 1000, Metravib, France) was used in this study to determine the dynamic mechanical properties of mortars. The variation curves of storage modulus (E'), loss modulus (E'') and loss factor ($\tan\delta$) of the sample with time and frequency can be obtained by DMA test. The storage modulus reflects the ability of the specimen to store mechanical energy during the action of stress. It is usually associated with the stiffness of a material and is considered to be related to Young's modulus. In contrast, the loss modulus is a viscous response of the material, which represents the energy dissipated by the sample under the stress. The loss factor is defined as the ratio of loss modulus to storage modulus. A higher loss factor indicates higher inelastic deformation, while a lower value indicates higher elastic deformation. Each E', E'', and $\tan\delta$ were derived from the following equations:

$$E' = \sigma_0 \cos\delta/\varepsilon_0 E'' = \sigma_0 \sin\delta/\varepsilon_0 \tag{4}$$

$$\tan\delta = \frac{1}{2\pi}\frac{\Delta w}{w} = E''/E' \tag{5}$$

$$\Delta w = \pi\varepsilon_0^2 E'' \tag{6}$$

$$w = \frac{1}{2}\varepsilon_0^2 E' \tag{7}$$

$$M^* = E'(1 + i\tan\delta) \tag{8}$$

where E' is the elastic modulus or storage modulus, E'' is the viscous modulus or loss modulus, σ_0 is the stress, Δw is the energy consumed in one cycle of material vibrates, w is the maximum strain energy stored by the material for one cycle, ε_0 is the strain, and δ is the phase angle, M^* is the complex modulus.

For earthquakes, low-frequency waves in the range of 1–10 Hz may cause serious damage to the infrastructure construction. Depending on the geological conditions, they can travel considerable distances and may match the resonant fundamental frequency of buildings (Achaoui et al., 2017). Thus, it is necessary to study the dynamic mechanical properties of cement-based materials in that range. According to the previous studies (Liu et al., 2018; Ou et al., 2008), the vibration frequency was usually set below 2 Hz. In this study, the vibration frequency was set at 0.5–2 Hz. Besides, the static force was set at −100 N, and the maximum dynamic force was set at 80 N. As shown in Fig. 6, the 30 × 30 × 30 mm^3 specimens for the DMA test were cut from the middle of 40 × 40 × 160 mm^3 specimens, so that the DMA specimens can reflect the correct information of fiber distribution.

2.3.6. Pore structure measurement

BJH (Barrett-Joyner-Halenda) method was used to characterize the

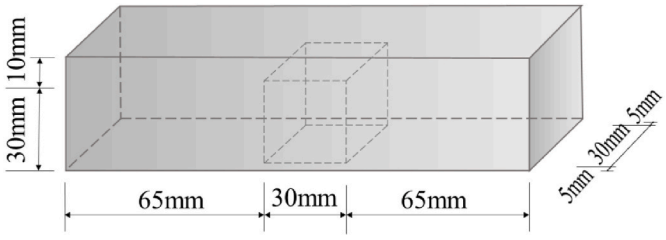

Fig. 6. Relationship between the specimens with different Dimensions.

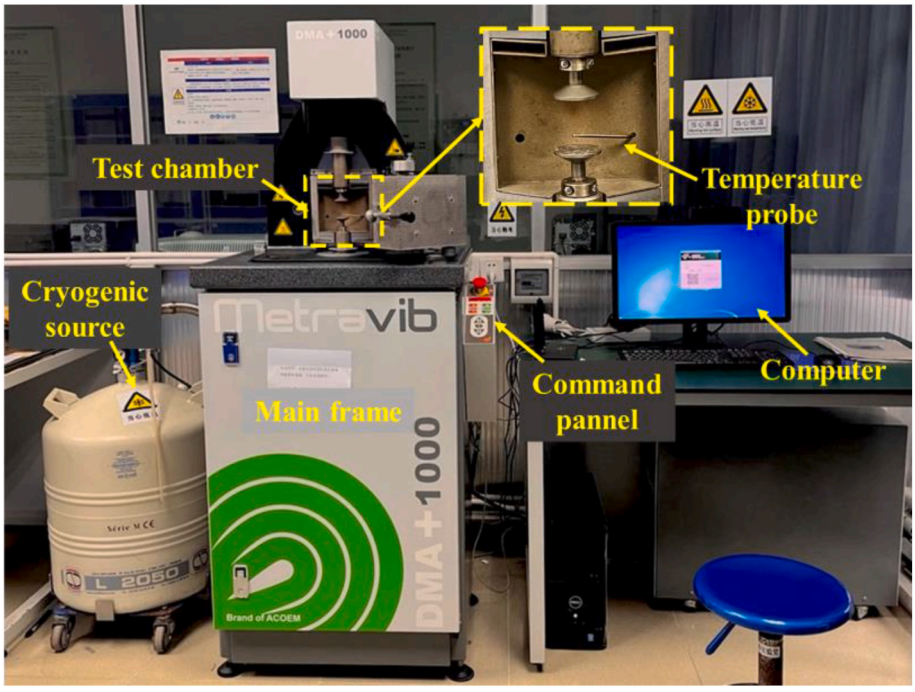

Fig. 5. Test setup of the dynamic mechanical analyzer.

pore size distributions and pore volume of mixtures with nitrogen adsorption techniques on a TriStar II 3020 instrument (Panesar and Francis, 2014; Snoeck et al., 2015). Before testing, the binders were crushed into granular samples with a diameter of 1–2 mm and dried to constant mass in a vacuum oven at 60 °C. For each group, 56 equilibrium points were collected during adsorption and desorption.

2.3.7. SEM observation

A Quanta 200 FEG was used to evaluate the fiber-matrix interface. Specimens of 10 × 10 × 10 mm^3 with an embedded fiber were cut from the dog-bone-shaped specimens. The samples were soaked in Ethanol absolute for 48 h to stop hydration and then dried to constant mass in a vacuum oven at 60 °C. The specimens were coated with a thin layer of gold (1 nm) after the surface of the specimens was polished. SEMs were recorded at a voltage of 20 kV and different magnifications.

To better understand this study, a research flow chart is provided in Fig. 7. In general, the fresh properties, hardening properties, ecological and economic efficiency of FRMs with different binder systems were studied.

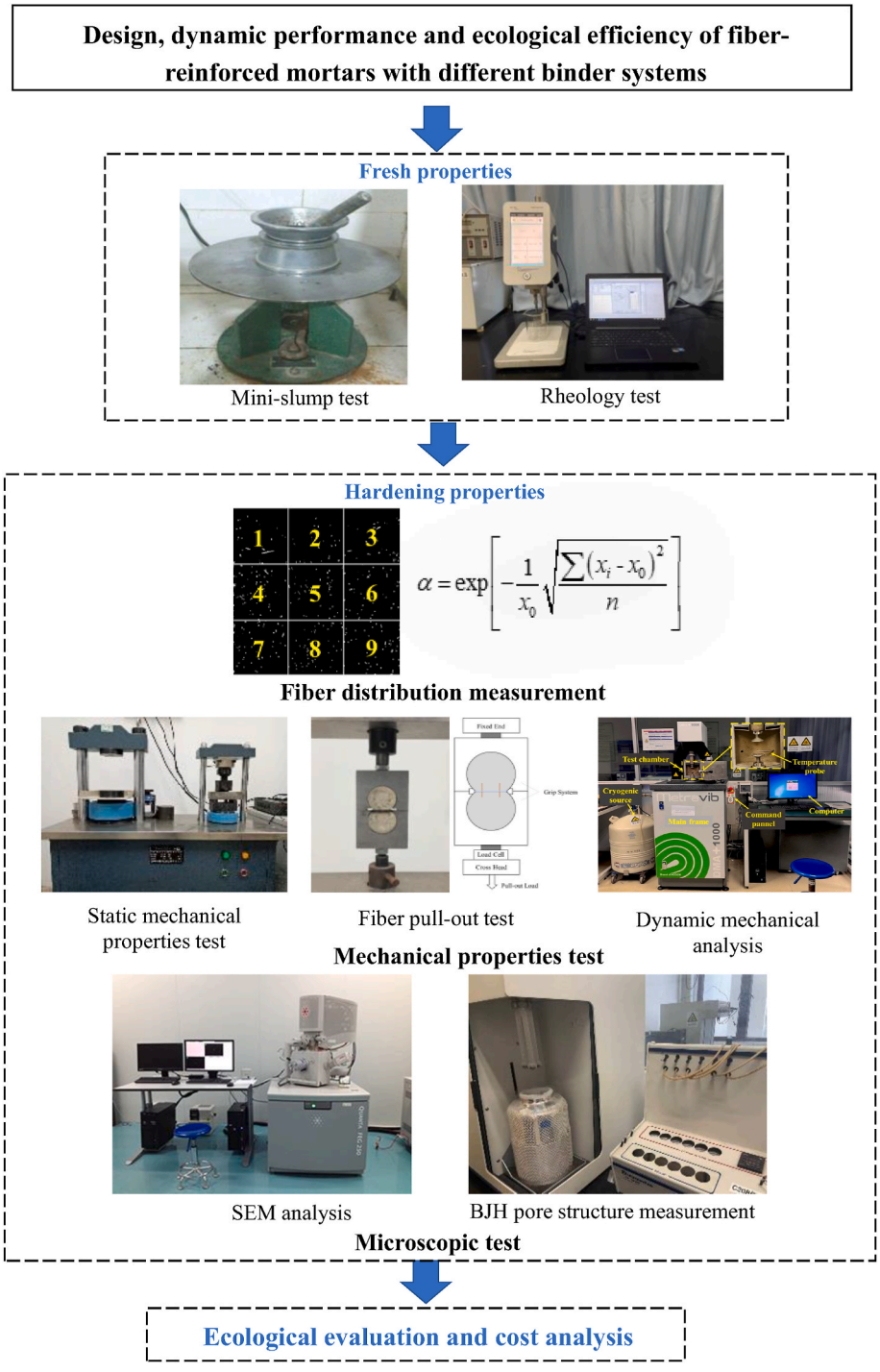

Fig. 7. Research flow chart of this study.

3. Results and discussions

3.1. Fresh properties

The mini-slump flow and rheological properties of all mixtures are summarized in Table 4. The mini-slump flow of all mixtures was controlled 250 ± 5 mm. The yield stress and plastic viscosity of different mixtures were calculated according to the relationship between shear stress and shear rate, based on the Bingham model, as shown in Fig. 8. The yield stress and plastic viscosity of AASM, as the benchmark in rheological control, were 17.34 Pa and 4.36 pa·s, respectively. To be consistent with the rheological properties of AASM, different contents of HRWR and HPMC were used to adjust the rheological parameters of FRMs made with OPC and LC^3. As a result, the yield stress and plastic viscosity of three kinds of mixtures were all 16 ± 1.6 Pa and 4 ± 0.4 Pa s. This would lead to fiber distribution at the same range in different kinds of mixtures, as previous studies have shown that there is a corresponding relationship between fiber distribution and the rheological properties of mixtures (Jasiuniene et al., 2018; Wang et al., 2017).

The result of OPC-1 and LC^3-1 also indicates that to maintain the same mini-slump flow, the content of HRWR in LC^3-1 was 4.65 times that of OPC-1 at a specific W/B ratio. The reason for this is that the increase in fineness of calcined clay increased the saturation point of HRWR, which was confirmed by Ferreiro et al. (2017). It is worth noting that the yield stress also changed with the addition of HPMC while adjusting the viscosity of FRMs made with OPC and LC^3 (Chen et al., 2018; Zhi et al., 2018). As a consequence, a higher content of HRWR was required to maintain the yield stress of OPC-2 and LC^3-2.

3.2. Fiber distribution

Fig. 9 shows the fiber distribution of all mixtures before and after adjusting the rheological parameters. The RGB images were converted to a binary image using ImageJ software. As shown in Fig. 9, the fiber distribution was non-uniform in the mortars with low plastic viscosity, especially for OPC-1. This was because that the paste could not hold the fiber at low viscosity, leading to agglomeration and settlement of fiber (Meng and Khayat, 2017). It can also be found that the fiber distribution coefficient (α) of FRMs made with OPC and LC^3 increased from 0.34 to 0.69, and from 0.52 to 0.72 when the viscosity increased from 0.73 Pa s to 4.17 Pa s, and from 1.09 Pa s to 3.86 Pa s respectively. The result indicates that the fiber distribution can be improved by increasing the plastic viscosity of mortars, which was in agreement with the investigation by Teng et al. (2020). Furthermore, the α of these mortars can be considered the same in this study since the difference was lower than 0.05.

3.3. Static mechanical properties

The static mechanical properties of different kinds of mortars at 28d was shown in Fig. 10. Both compressive and flexural strength of the three kinds of mixtures showed the same trend that AASM > LC^3-2>OPC-2. The compressive strength of AASM was 52.2% and 36.3% higher than that of OPC-2 and LC^3-2, while the flexural strength of AASM was 17.0% and 4.0% higher than that of OPC-2 and LC^3-2. This

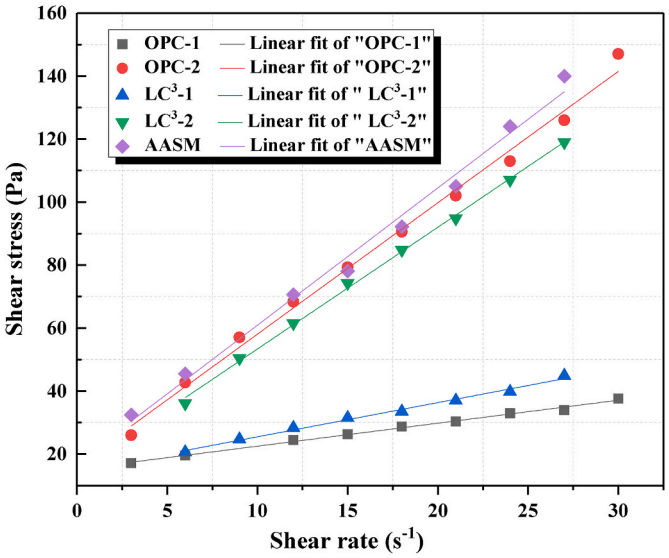

Fig. 8. Flow curves of different mixtures.

can be attributed to the denser matrix of AASM compared with FRMs made with OPC and LC^3, which will be discussed in Section 3.6. With the addition of HPMC, the compressive strength of FRMs made with OPC and LC^3 decreased by 12.6% and 8.6% respectively, mainly due to the greater entrapped air in the matrix caused by a higher viscosity (Tosun-Felekoglu et al., 2014). However, as the viscosity increased, the flexural strength of FRMs made with OPC and LC^3 increased by 9.8% and 9.6% respectively, as the fiber distribution coefficient of FRMs made with OPC and LC^3 increased from 0.34 to 0.69, and from 0.52 to 0.72 respectively. Better fiber distribution can offset the disadvantage of increased porosity and increase the possibility of fiber to bridge the matrix cracks, thus the flexural strength of FRMs improved. This result was confirmed by the findings of Meng and Khayat (2017) and Teng et al. (2020).

3.4. Fiber pull-out test

Fig. 11 (a) shows the pull-out load-slip curves of different kinds of mortars at 28d. All curves show that the pull-out load first increased and then decreased with the increase of slip, which was corresponding to the process of fiber gradually pulling out from the matrix. According to the load-slip curves, the bond strength and pull-out energy of all specimens can be calculated, as shown in Fig. 11 (b). The results show that the bond strength of fiber embedded in the AASM matrix was 1.40 MPa, 88.9%, and 34.5% higher than that in the OPC-2 and LC^3-2 matrix, respectively. In addition, the bond strength of fiber embedded in OPC and LC^3 matrix decreased by 28.4% and 9.3% respectively after adding HPMC. However, this defect was compensated by better fiber distribution and thus the flexural performances of FRMs made with OPC and LC^3 were still improved.

The pull-out energy was obtained by integrating the area under the load-slip curves. In general, the pull-out energy shows a similar trend to

Table 4
Fresh properties of mixtures.

Mix ID	OPC-1		OPC-2		LC^3-1		LC^3-2		AASM	
	Mean	COV%	Mean	COV%	Mean	COV%	Mean	COV%	Mean	COV%
HRWR (%)[a]	0.20	-	1.20	-	0.93	-	1.50	-	-	-
Mini-slump flow(mm)	250	3.7	245	5.6	250	4.2	250	2.5	245	4.8
Yield stress (Pa)	15.2	1.3	16.4	1.5	14.6	2.4	14.7	3.1	17.3	2.1
Plastic viscosity (Pa·s)	0.7	2.0	4.2	1.7	1.1	1.4	3.9	2.1	4.4	1.8

[a] Active portion, by mass of binder.

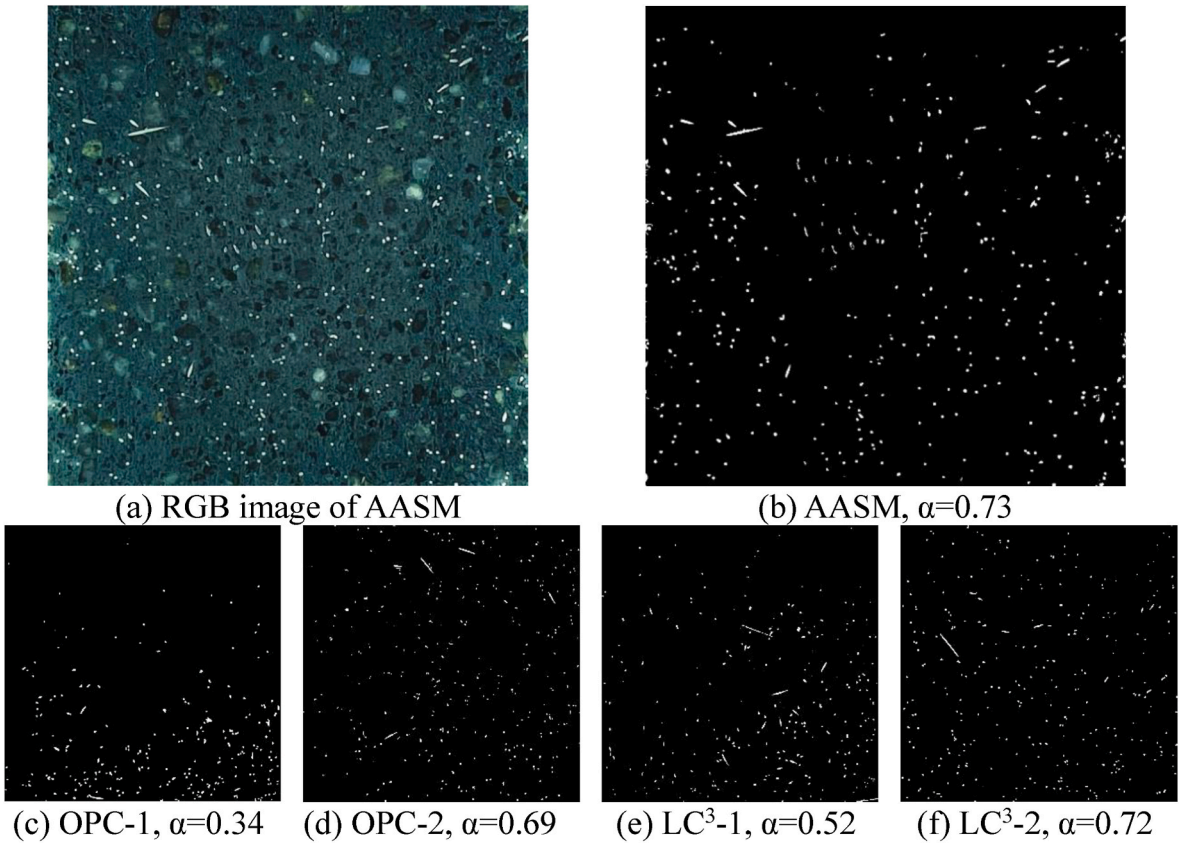

Fig. 9. Binary images of all mixtures.

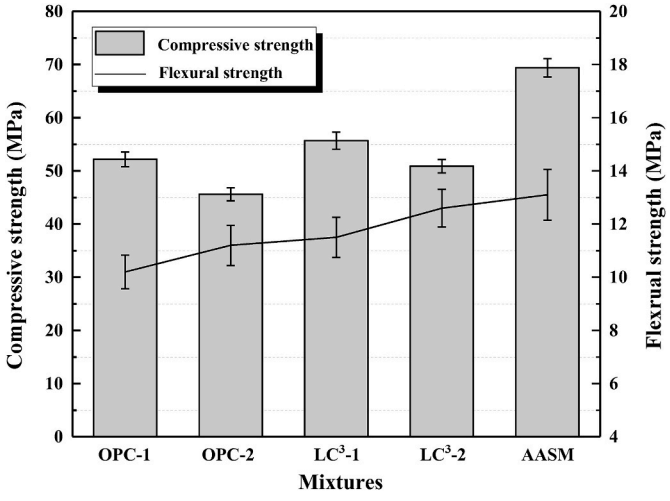

Fig. 10. Compressive and flexural strength of mortars at 28d.

the bond strength. The pull-out energy of fiber embedded in the AASM matrix (44.54 N-mm) was 104.6% and 48.0% higher than that in the OPC-2 and LC^3-2 matrix, respectively. With the addition of HPMC, the pull-out energy of fiber embedded in the OPC and LC^3 matrix also decreased by 18.5% and 25.1%, respectively. The results of the fiber pull-out test indicate that the bond strength and pull-out energy are positively related to the strength of the matrix, which is consistent with the findings of Kim et al. (2017) and Le et al. (2018).

3.5. Dynamic mechanical properties

3.5.1. Storage modulus

The storage modulus is associated with the stiffness of materials and directly reflects the energy storage capacity of materials under the action of stress (Muthusamy et al., 2010). Fig. 12 illustrates the 28-day storage modulus of all mortars at a different frequency (0.5–2 Hz) and test time. It can be found that the storage modulus of AASM was the highest, 80% and 150% higher than that of LC^3-2 and OPC-2 respectively. This indicates that AASM had the best ability to store energy under the action of dynamic load among the three kinds of mortars due to its lowest porosity, which resulted in a denser matrix and higher stiffness. Fig. 12(a) also indicates that the storage modulus of all kinds of mortars reached the highest at 0.5Hz. With the further increase of frequency, the storage modulus remained at a certain level. This finding is consistent with the previous studies (Li et al., 2020; Long et al., 2018), where the optimum frequency of 0.5Hz for storage modulus was also reported.

It can also be found in Fig. 12(a) that the storage modulus of FRMs made with OPC and LC^3 decreased by 12.6% and 25.0% respectively with the addition of HPMC, as the HPMC significantly increased the viscosity of mortars and resulted in the increment of porosity. This indicates that the improvement of fiber distribution in FRMs made with OPC and LC^3 (shown in Fig. 9) had no obvious positive effect on the storage modulus, or this effect was slighter than the negative effect caused by the increase of porosity. The results of storage modulus are consistent with that of the compressive strength test.

3.5.2. Loss factor

The loss factor was measured to characterize the damping capacity of mortars (Leiben et al., 2018). The higher the loss factor, the greater the phase displacement between the given stress and the measured strain of

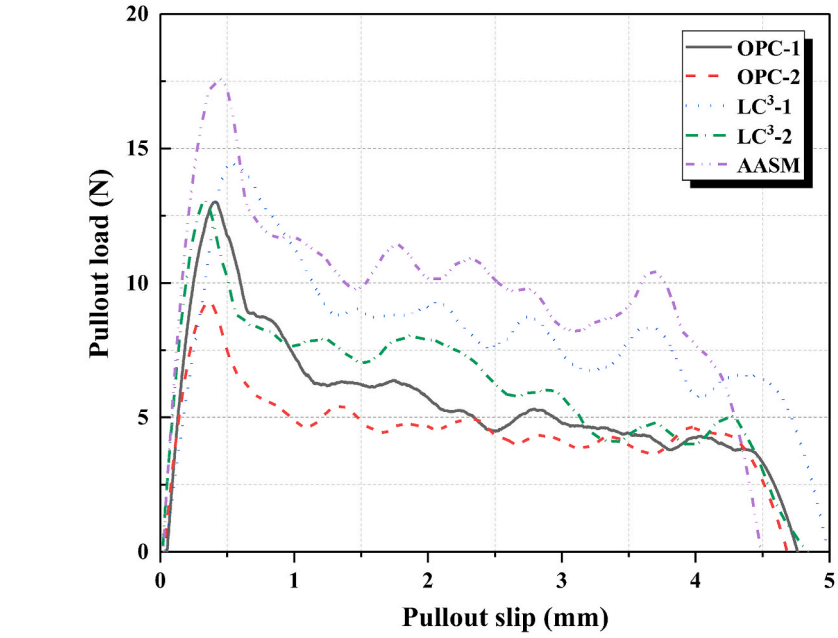

(a) load-slip curves

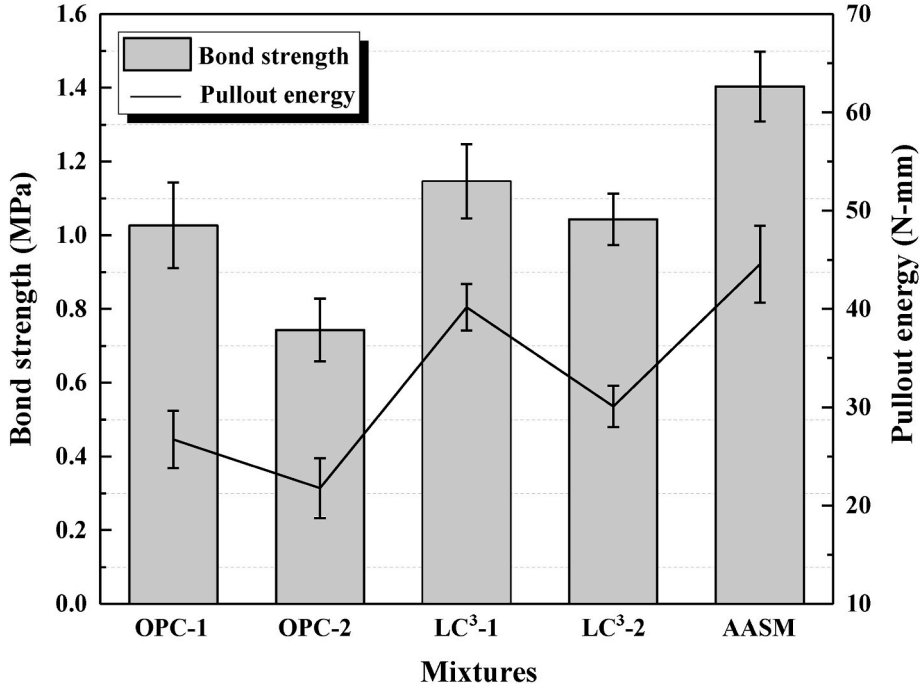

(b) bond strength and pull-out energy

Fig. 11. Fiber pull-out behavior of mortars at 28d.

mortars, which means better damping capacity. Fig. 13 illustrates the 28-day loss factor of all mortars. It can be found in Fig. 13 (a) that the loss factor of LC^3-2 was 0.076 at 0.5 Hz, 70% and 150% higher than that of OPC-2 and AASM respectively. This indicates that when the fiber distributions were consistent, LC^3-2 had the best damping capacity among the three kinds of mortars. Compared with OPC-2, the matrix and the ITZ between fiber and matrix in LC^3-2 were denser (shown in Fig. 14), which effectively reduced the possibility of defects in the matrix and was conducive to energy dissipation. As a consequence, the loss factor of LC^3-2 was higher than OPC-2. However, the loss factor of AASM was the lowest among the three kinds of mortars, while the matrix of AASM was the densest (shown in Fig. 14). This was attributed to the over-high stiffness of the AASM matrix which led to poor deformation ability under the action of dynamic load (Long et al., 2017a). Unlike the storage modulus, Fig. 13 (a) indicates that the loss factor of all groups hardly changed with the increase of frequency. This means that the loss factor was insensitive to the frequency ranging from 0.5–2 Hz.

It can also be found in Fig. 12 (a) that the loss factor of FRMs made with OPC and LC^3 increased significantly with the increase of the plastic viscosity. This was partly due to the improvement of fiber distribution. The bridging effect of fibers on cracks in the matrix can significantly improve the damping capacity of mortars (Zhang et al., 2020; Zhao et al., 2020). As the fiber distribution became more uniform with the increase of viscosity, fibers were more likely to bridge more cracks and

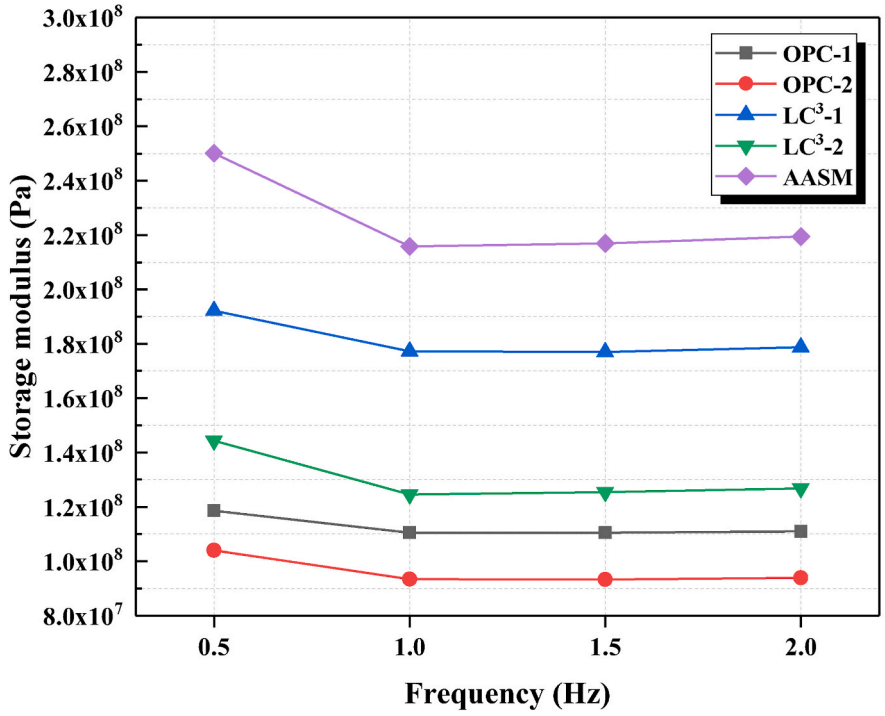

(a) Storage modulus with different frequency

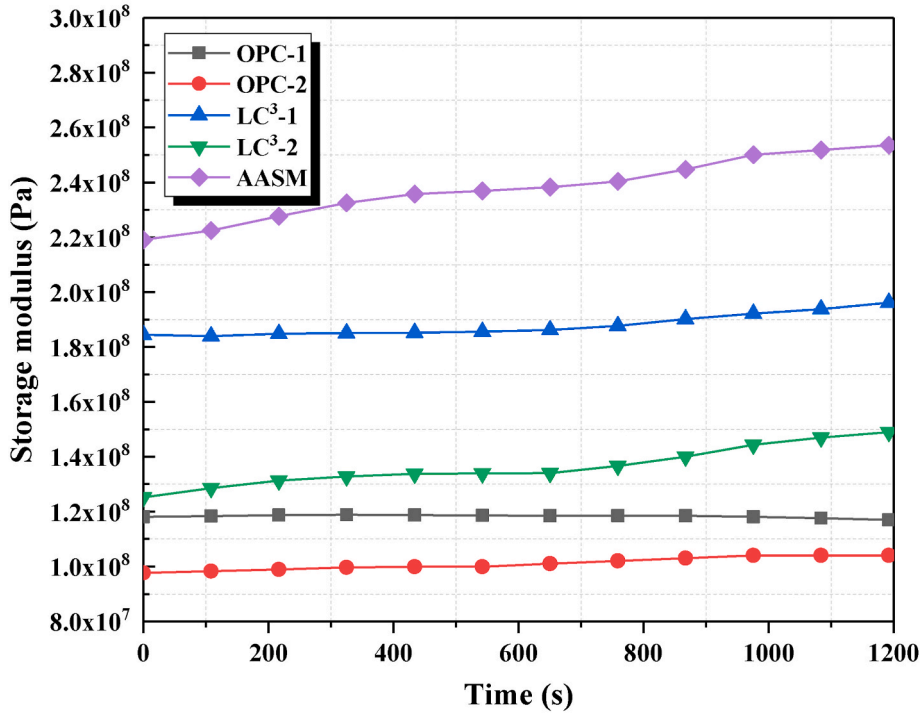

(b) Storage modulus with different test time at 0.5Hz

Fig. 12. Storage modulus of mortars at 28d with different frequency and test time.

further improved the damping capacity of mortars. Thus, the loss factor of FRM made with OPC increased by 25.0% as the fiber distribution coefficient increased from 0.34 to 0.69, and the loss factor of FRM made with LC^3 increased by 8.6% as the fiber distribution coefficient increased from 0.52 to 0.72. Besides, the increase of loss factor was also attributed to the change of pore structure, as the increase of pores in a certain range can work as a cushion to improve the damping capacity of mortars (Liu et al., 2010). It should be noted that the deterioration of the fiber-matrix interfacial bond properties was disadvantageous to the damping capacity of mortars, but this negative effect was offset by the positive effect of fiber distribution and pore structure improvement.

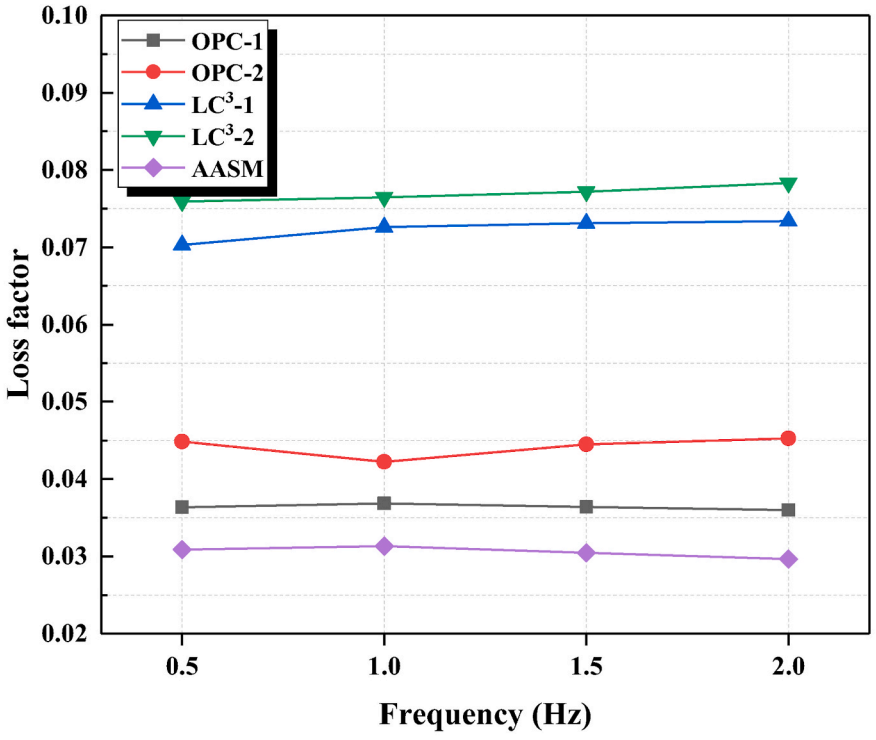

(a) Loss factor with different frequency

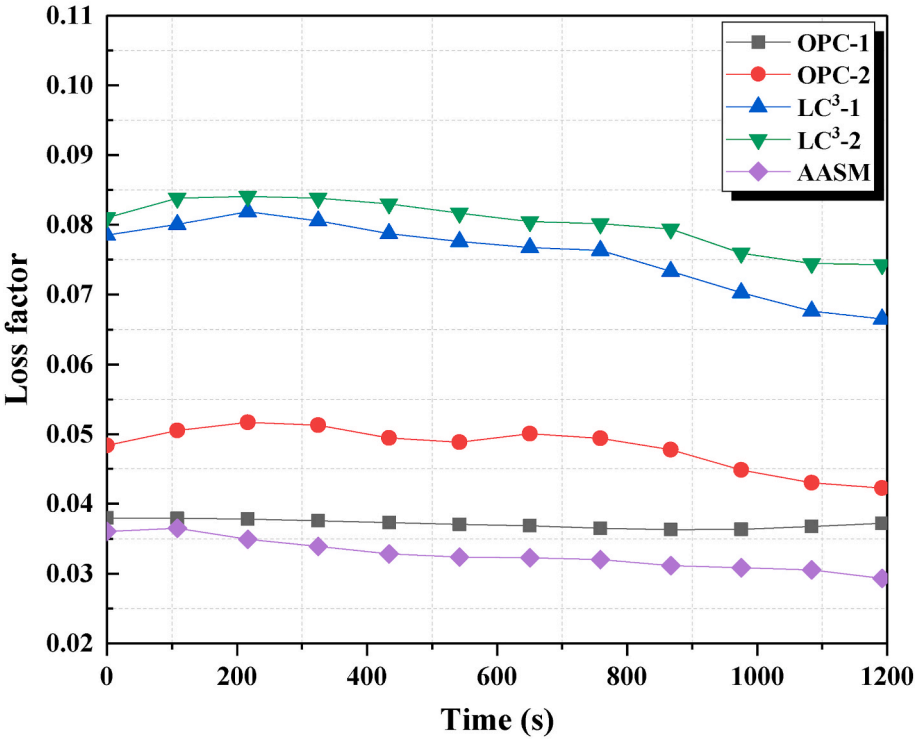

(b) Loss factor with different test time at 0.5Hz

Fig. 13. Loss factor of mortars at 28d with different frequency and test time.

3.6. Pore structure

The pore size distributions of mortars at 28d are shown in Fig. 14. For AASM, a higher volume of pores from 2.6 nm to 3.8 nm and a lower volume of pores larger than 27 nm was observed. This indicates that the matrix of AASM was the densest because most of the pore diameter in the AASM matrix was lower than 3.8 nm as the pore diameter in the matrix was lower than 50 nm. The densest matrix of AASM led to the highest compressive strength and storage modulus, but also the poorest damping capacity, for a too dense matrix was disadvantageous to damping capacity (Long et al., 2017a). Notably, appropriate matrix density is advantageous to damping ability, as the loss factor of LC^3-2

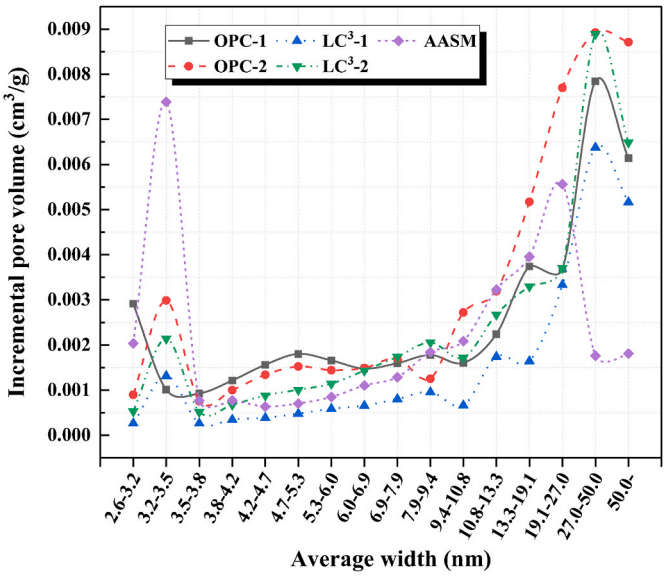

Fig. 14. Pore size distributions of mortars at 28d.

was higher than OPC-2. Fig. 14 also showed that the porosity of FRMs made with OPC and LC^3 increased with the addition of HPMC. This was because that the air bubbles are entrained and difficult to escape during the mixing process due to the increase of viscosity of mortars. The effect of these bubbles was similar to that of air cushion, which provided a buffer for the matrix under dynamic load and thus enhanced the damping capacity of the matrix (Liu et al., 2010).

3.7. SEM analysis

Fig. 15 shows the SEM images of the fiber-matrix interface of mortars. It can be found that the matrix of LC^3-2 around the embedded fiber was dense and homogenous, due to the filling effect of fine particles of calcined clay. This means that the fiber-matrix interfacial properties of LC^3-2 were satisfactory, which had been verified in the fiber pull-out testing. Good fiber-matrix interfacial properties ensure the energy dissipation under dynamic load (Zhang et al., 2017), as a consequence, the damping capacity of LC^3-2 were good. However, though the fiber-matrix interfacial properties of AASM were also good, the damping capacity of AASM were not satisfactory due to the over-dense and large brittleness of the AASM matrix (Long et al., 2017a), as shown in Fig. 15 (b).

It can also be found in Fig. 15 (c) that a lot of pores and microcracks were surrounding the fibers in the OPC-2. The possible reason for this is that the particle size of cement is larger than that of calcined clay and slag, and its filling effect on the fiber-matrix interface is not as good as that of calcined clay and slag. As a consequence, the fiber-matrix interfacial properties of OPC-2 were poorer than that of LC^3-2 and AASM.

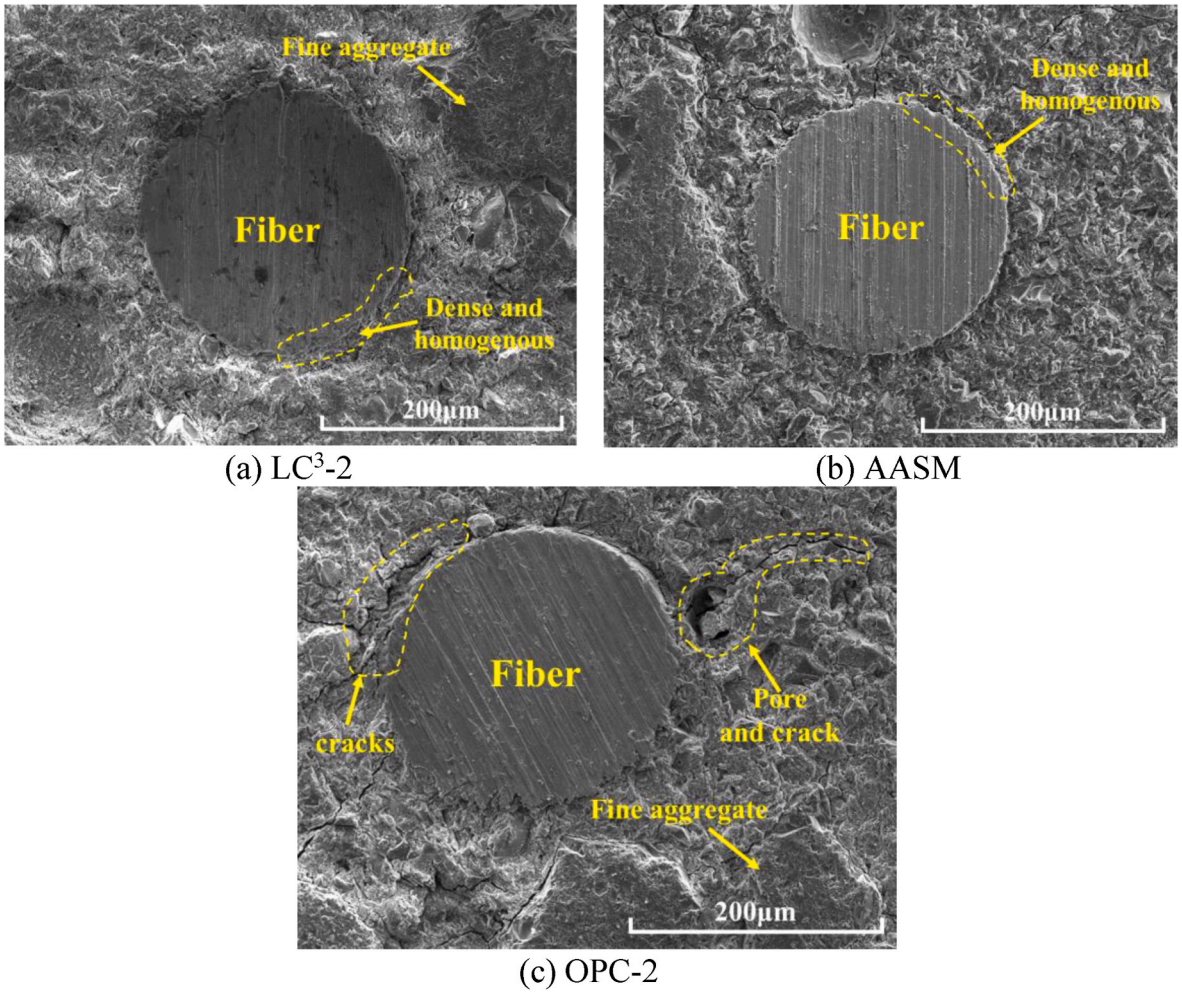

Fig. 15. SEM images of fiber-matrix interface of mortars.

4. Ecological evaluation and cost analysis of mixtures

It should be noted that the comparison of the three kinds of mixtures should not stay at the level of dynamic mechanical properties. That is to say, it's also necessary to compare the ecological and economic efficiency of mixtures. This will help to recommend one kind of mixture with better dynamic mechanical properties, environmental protection and lower cost. In this section, the ecological evaluation was conducted by life cycle assessments (LCA), based on ISO 14040-2006. Two parameters, Embodied energy (EE) and Embodied carbon dioxide emissions (ECO_2e), were introduced to evaluate the ecological efficiency of the three kinds of mixtures. EE represents the amount of consumed energy, while ECO_2e represents the CO_2 emissions during the process of raw material extraction, manufacturing, assembly, installation, disassembly, transportation, and deconstruction of any given product system during the product's life (Faridmehr et al., 2021; Yaragal et al., 2020). Table 5 shows the basic parameters of EE, ECO_2e, and the cost of each raw material used in this study, which was used to calculate the total EE, ECO_2e, and the costs of different kinds of mixtures. The united values of EE and ECO_2e for various raw materials were obtained from the Ecoinvent Database and literature (Long et al., 2020; Yu et al., 2021; Yudiesky Cancio Díaz a et al., 2017). Moreover, the costs of the three kinds of mixtures were analyzed based on the prices of the materials from Shenzhen, China.

As a characterization of damping capacity of materials, the loss factor can well reflect the dynamic mechanical properties of mixtures. To comprehensively evaluate the dynamic mechanical properties, ecological and economic efficiency of mixtures, the EE, ECO_2e and the cost of unit loss factor of different kinds of mixtures were introduced and further compared.

Fig. 16 shows the EE, ECO_2e and the cost of unit loss factor of different kinds of mixtures, among which LC^3-2 had the lowest values, showing 48369.1 MJ/m^3, 6894.4 $kgCO_2/m^3$, and 20288.0 RMB/m^3 respectively. Compared with OPC-2, the above parameters were reduced by 55.8%, 66.9%, and 46.0% respectively. As for AASM, the EE and ECO_2e of unit loss factor were reduced by 10.0% and 46.6% compared with OPC-2, while the cost of unit loss factor increased by 15.0%. This indicates that LC^3-2 had the most significant ecological and economic efficiency among the three kinds of mixtures under certain damping capacity.

Besides, Fig. 16 also shows the proportion of the EE, ECO_2e, and the cost of each raw material. It can be found that cement had the greatest impact on EE and ECO_2e of OPC-2 (Hu et al., 2020; Kulasuriya et al., 2021), as the cement accounted for 93.7% and 85.1% of the EE and ECO_2e of OPC-2, respectively. For AASM, the effect of activator (LSS and NaOH) on EE and ECO_2e was significant, accounting for 50.2% of the total EE and 41.7% of the total ECO_2e, respectively. In general, LC^3-2 was more environmentally friendly and economically efficient under the same damping capacity, compared with OPC-2 and AASM. Thus, LC^3-2 was recommended as the cleaner product of fiber-reinforced mortars with good dynamic loadings resistance.

Table 5
EE, ECO_2e, and cost of basic parameters.

Components	Data for each material		
	EE (MJ/kg)	ECO_2e ($kgCO_2/kg$)	Cost (RMB/kg)
Cement	5.5	0.95	0.78
Ground clinker	5.5	0.74	0.75
Calcined clay	2.734	0.196	0.45
Limestone	0.85	0.032	0.3
Gypsum	1.8	0.12	0.2
Slag	1.6	0.083	0.31
Water	0.2	0.0008	0.007
HRWRA	11.5	0.75	8.0
HPMC	2.56	0.24	2.36
NaOH	20.5	0.7458	2.5
LSS	10.2	1.237	0.65
River Sand	0.081	0.0051	0.06
Steel fiber	0.15	1.4965	10.5

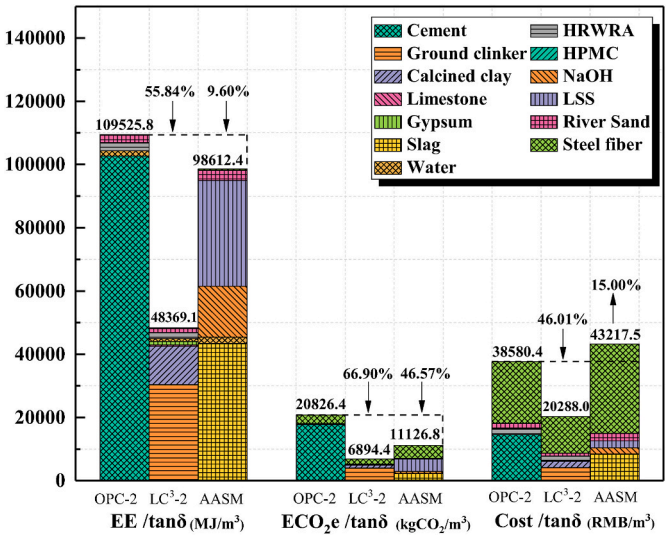

Fig. 16. Proportion of EE, ECO_2e and cost of each raw material.

5. Conclusions

In this study, the dynamic mechanical properties, ecological and economic efficiency of fiber-reinforced mortars with three types of binder systems (OPC, LC^3, and AAS) were compared. In addition, the effect of the rheological parameter of FRMs on dynamic response was also investigated. The following conclusions can be drawn:

(1) The storage modulus of AASM was the highest, followed by LC^3-2 and OPC-2, meaning that AASM had the best ability to store energy among three kinds of mortars due to its lowest porosity and highest stiffness, as the plastic viscosity of mixtures was at the same range.

(2) The loss factor of LC^3-2 was the highest, followed by OPC-2 and AASM, meaning that LC^3-2 had the best damping capacity among the three kinds of mortars. This was contributed to the appropriate pore size distributions and fiber-matrix interfacial properties of LC^3-2, as the plastic viscosity of mixtures was at the same range.

(3) The improvement of plastic viscosity significantly improved the damping capacity of FRMs, as the loss factor increased by 25.0% and 8.6% in FRMs made with OPC and LC^3 respectively. This was attributed to the higher plastic viscosity which resulted in better fiber distribution in the FRMs.

(4) The bond strength and pull-out energy of fiber embedded in the AASM matrix were the highest, 88.9% and 104.6% higher than that in the OPC-2 matrix, 34.5% and 48% higher than that in the LC^3-2 matrix, respectively. The bond strength and pull-out energy of fiber embedded in OPC and LC^3 matrix decreased by 28.4% and 9.3%, by 18.5% and 25.1%, respectively, as the plastic viscosity increased. However, a better fiber distribution can compensate for this defect.

(5) The results of BJH testing and SEM confirmed that the interface between fiber and matrix in AASM was denser than that in OPC-2 and LC^3-2. This was because that most of the pore diameter in the AASM matrix was lower than 3.8 nm as the pore diameter in the matrix was lower than 50 nm. However, the effect of pore structure was similar to that of air cushion, which provided a buffer for the matrix under dynamic load and thus enhanced the damping capacity of OPC-2 and LC^3-2.

(6) The EE, ECO_2e, and the cost of unit loss factor of LC^3-2 were the lowest among all mortars made with three kinds of binder systems. Compared with OPC-2, the above parameters of LC^3-2 were reduced by 55.8%, 66.9%, and 46.0% respectively. This indicated that the FRM made with LC^3 had the best dynamic mechanical properties, environmental protection and lowest cost among the three kinds of mortars.

CRediT authorship contribution statement

Wu-Jian Long: Experimental design, supervision and manuscript reviewing, Supervision, Writing – review & editing. **Zhuorui Wu:** Data collection, Data curation, Writing – original draft. **Kamal H. Khayat:** Writing – review & editing, Supervision, Writing – review & editing, supervision and editing. **Jingjie Wei:** Experimental design, Supervision, Writing – original draft, Writing – review & editing. **Biqin Dong:** Visualization, Investigation. **Feng Xing:** Writing – review & editing. **Jinrui Zhang:** Writing – review & editing.

Declaration of competing interest

The authors declare that they have no known competing financial interests or personal relationships that could have appeared to influence the work reported in this paper.

Acknowledgement

The authors gratefully acknowledge the financial support provided by the National Natural Science Foundations of China, NSFC-Shandong Joint Fund (No. U2006223), the Science and Technology Project of Shenzhen, China (No. JCYJ20190808151011502 and No. JCYJ20180305124844894), and the Guangdong Provincial Key Laboratory of Durability for Marine Civil Engineering (SZU) (No. 2020B1212060074), as well as the Center for Infrastructure Engineering Studies (CIES) and Advanced Construction and Material Laboratory (ACML) at Missouri University of Science and Technology.

References

Achaoui, Y., Antonakakis, T., Brule, S., Craster, R.V., Enoch, S., Guenneau, S., 2017. Clamped seismic metamaterials: ultra-low frequency stop bands. New J. Phys. 19, 13.
Aghaeipour, A., Madhkhan, M., 2017. Effect of ground granulated blast furnace slag (GGBFS) on RCCP durability. Construct. Build. Mater. 141, 533–541.
Alberti, M.G., Enfedaque, A., Galvez, J.C., Agrawal, V., 2016. Fibre distribution and orientation of macro-synthetic polyolefin fibre reinforced concrete elements. Construct. Build. Mater. 122, 505–517.
Amran, M., Murali, G., Khalid, N.H.A., Fediuk, R., Ozbakkaloglu, T., Lee, Y.H., Haruna, S., Lee, Y.Y., 2021. Slag uses in making an ecofriendly and sustainable concrete: a review. Construct. Build. Mater. 272.
Ashish, D.K., 2019. Concrete made with waste marble powder and supplementary cementitious material for sustainable development. J. Clean. Prod. 211, 716–729.
Ayub, T., Khan, S.U., Memon, F.A., 2014. Mechanical characteristics of hardened concrete with different mineral admixtures: a review. Sci. World J. 2014, 1–15.
Behfarnia, K., Rostami, M., 2017. Mechanical properties and durability of fiber reinforced alkali activated slag concrete. J. Mater. Civ. Eng. 29 (12).
Benhelal, E., Zahedi, G., Shamsaei, E., Bahadori, A., 2013. Global strategies and potentials to curb CO2 emissions in cement industry. J. Clean. Prod. 51, 142–161.
CECS13, 2009. Standard test methods for fiber reinforced concrte. China. Assoc. Eng. Constr. Stand. 67–71.
Chen, M.X., Li, L.B., Zheng, Y., Zhao, P.Q., Lu, L.C., Cheng, X., 2018. Rheological and mechanical properties of admixtures modified 3D printing sulphoaluminate cementitious materials. Construct. Build. Mater. 189, 601–611.
Dehdezi, P.K., Erdem, S., Blankson, M.A., 2015. Physico-mechanical, microstructural and dynamic properties of newly developed artificial fly ash based lightweight aggregate - rubber concrete composite. Compos. B Eng. 79, 451–455.
Dhandapani, Y., Sakthivel, T., Santhanam, M., Gettu, R., Pillai, R.G., 2018. Mechanical properties and durability performance of concretes with limestone calcined clay cement (LC3). Cement Concr. Res. 107, 136–151.
Farhan, N.A., Sheikh, M.N., Hadi, M.N.S., 2018. Engineering properties of ambient cured alkali-activated fly ash-slag concrete reinforced with different types of steel fiber. J. Mater. Civ. Eng. 30 (7).
Faridmehr, I., Nehdi, M.L., Nikoo, M., Huseien, G.F., Ozbakkaloglu, T., 2021. Life-cycle assessment of alkali-activated materials incorporating industrial byproducts. Materials 14 (9).
Ferreiro, S., Herfort, D., Damtoft, J.S., 2017. Effect of raw clay type, fineness, water-to-cement ratio and fly ash addition on workability and strength performance of calcined clay - limestone Portland cements. Cement Concr. Res. 101, 1–12.
GB/T175, 2007. Common Portland Cement. China. Natl. Test. Stand., pp. 2–6
GB/T2419, 2005. Test method for fluidity of cement mortar. China. Natl. Test. Stand. 3–5.
GB/T14684, 2011. Sand for construction. China. Natl. Test. Stand. 2–6.
GB/T17671, 1999. Method of testing cements-Determination of strength. China. Natl. Test. Stand. 5–17.
GB/T18046, 2017. Ground granulated blast furnace slag used for cement, mortar and concrete China. Natl. Test. Stand. 1–18.
Gupta, N., Siddique, R., Belarbi, R., 2021. Sustainable and greener self-compacting concrete incorporating industrial by-products: a review. J. Clean. Prod. 284, 21.
Hu, L.L., He, Z., Zhang, S.P., 2020. Sustainable use of rice husk ash in cement-based materials: environmental evaluation and performance improvement. J. Clean. Prod. 264.
Huang, K., Ma, Q.Y., Ma, D.D., 2020. Effect of basalt fiber on static and dynamic mechanical properties of metakaolin-based cement clay. Adv. Civ. Eng. 2020, 1–14.
Jaiswal, K., Bausch, D., Rozelle, J., Holub, J., McGowan, S., 2017. Hazus® Estimated Annualized Earthquake Losses for the United States.
Jasiuniene, E., Cicenas, V., Grigaliunas, P., Rudzionis, Z., Navickas, A.A., 2018. Influence of the rheological properties on the steel fibre distribution and orientation in self-compacting concrete. Mater. Struct. 51 (4).
Kaliyavaradhan, S.K., Ling, T.C., 2017. Potential of CO2 sequestration through construction and demolition (C & D) waste-An overview. J. CO2 Util. 20, 234–242.
Kang, S.T., Kim, J.H., Lee, B.Y., 2019. Effects of water reducing admixture on rheological properties, fiber distribution, and mechanical behavior of UHPFRC. Appl. Sci.-Basel. 9 (1), 13.
Khan, I., Shahzada, K., Bibi, T., Ahmed, A., Ullah, H., 2021. Seismic performance evaluation of crumb rubber concrete frame structure using shake table test. Structures 30, 41–49.
Kim, B.J., Yi, C., Ahn, Y.R., 2017. Effect of embedment length on pullout behavior of amorphous steel fiber in Portland cement composites. Construct. Build. Mater. 143, 83–91.
Kim, H.K., Park, I.S., Lee, H.K., 2014. Improved piezoresistive sensitivity and stability of CNT/cement mortar composites with low water-binder ratio. Compos. Struct. 116, 713–719.
Kulasuriya, C., Vimonsatit, V., Dias, W.P.S., 2021. Performance based energy, ecological and financial costs of a sustainable alternative cement. J. Clean. Prod. 287.
Le, H.V., Moon, D., Kim, D.J., 2018. Effects of ageing and storage conditions on the interfacial bond strength of steel fibers in mortars. Construct. Build. Mater. 170, 129–141.
Lee, H.S., Wang, X.Y., Zhang, L.N., Koh, K.T., 2015. Analysis of the optimum usage of slag for the compressive strength of concrete. Materials 8 (3), 1213–1229.
Leiben, Z., Wang, X., Wang, Z., Yang, B., Tian, Y., He, R., 2018. Damping characteristics of cement asphalt emulsion mortars. Construct. Build. Mater. 173, 201–208.
Li, H.D., Zhang, Q.M., Feng, G.L., Mei, L., Wang, Y.C., Long, W.J., 2020. Multi-scale improved damping of high-volume fly ash cementitious composite: combined effects of polyvinyl alcohol fiber and graphene oxide. Construct. Build. Mater. 260.
Li, Z.M., Lu, T.S., Chen, Y., Wu, B., Ye, G., 2021. Prediction of the autogenous shrinkage and microcracking of alkali-activated slag and fly ash concrete. Cement Concr. Compos. 117.
Liew, K.M., Sojobi, A.O., Zhang, L.W., 2017. Green concrete: prospects and challenges. Construct. Build. Mater. 156, 1063–1095.
Liu, J., Wang, D.M., 2017. Influence of steel slag-silica fume composite mineral admixture on the properties of concrete. Powder Technol. 320, 230–238.
Liu, S.H., Wang, Z.G., Li, X., 2014. Long-term properties of concrete containing ground granulated blast furnace slag and steel slag. Mag. Concr. Res. 66 (21), 1095–1103.
Liu, T.J., Song, W., Zou, D.J., Li, L., 2018. Dynamic mechanical analysis of cement mortar prepared with recycled cathode ray tube (CRT) glass as fine aggregate. J. Clean. Prod. 174, 1436–1443.
Liu, T.J., Xing, F., Sui, L.L., Zhang, F., 2010. Effect of air bubbles on damping behavior of fiber concretes. J. Funct. Mater. 41, 2140–2143.
Long, W.J., Li, H.D., Wei, J.J., Xing, F., Han, N.X., 2018. Sustainable use of recycled crumb rubbers in eco-friendly alkali activated slag mortar: dynamic mechanical properties. J. Clean. Prod. 204, 1004–1015.
Long, W.J., Tan, X.W., Xiao, B.X., Han, N.X., Xing, F., 2020. Effective use of ground waste expanded perlite as green supplementary cementitious material in eco-friendly alkali activated slag composites. J. Clean. Prod. 213, 406–414.
Long, W.J., Wei, J.J., Gu, Y.C., Xing, F., 2017a. Research on dynamic mechanical properties of alkali activated slag concrete under temperature-loads coupling effects. Construct. Build. Mater. 154, 687–696.
Long, W.J., Wei, J.J., Ma, H.Y., Xing, F., 2017b. Dynamic mechanical properties and microstructure of graphene oxide nanosheets reinforced cement composites. Nanomaterials 7 (12).
Luo, X., Xu, J.Y., Li, W.M., Wang, Z.K., 2015. Comparative study of the effect of basalt fiber on dynamic damage characteristics of ceramics cement-based porous Material. J. Mater. Civ. Eng. 27 (8).
Mastali, M., Kinnunen, P., Dalvand, A., Firouz, R.M., Illikainen, M., 2018. Drying shrinkage in alkali-activated binders - a critical review. Construct. Build. Mater. 190, 533–550.

Meng, W.N., Khayat, K.H., 2017. Improving flexural performance of ultra-high-performance concrete by rheology control of suspending mortar. Compos. B Eng. 117, 26–34.
Mohamed, O.A., 2019. A review of durability and strength characteristics of alkali-activated slag concrete. Materials 12 (8).
Muthusamy, S., Wang, S., Chung, D.D.L., 2010. Unprecedented vibration damping with high values of loss modulus and loss tangent, exhibited by cement-matrix graphite network composite. Carbon 48 (5), 1457–1464.
Ostovari, H., Mueller, L., Skocek, J., Bardow, A., 2021. From unavoidable CO2 source to CO2 sink? A cement industry based on CO2 mineralization. Environ. Sci. Technol. 55 (8), 5212–5223.
Ou, J.P., Liu, T.J., Li, J.L., 2008. Dynamic and seismic property experiments of high damping concrete and its frame models. J. Wuhan Univ. Technol.-Materials Sci. Ed. 23 (1), 1–6.
Pan, T.Y., Melgar, C., Robinson, T., 2012. Damping capacity of styrene-butadiene latex admixed concrete: a micromechanical study. J. Mater. Civ. Eng. 24 (9), 1237–1244.
Panesar, D.K., Francis, J., 2014. Influence of limestone and slag on the pore structure of cement paste based on mercury intrusion porosimetry and water vapour sorption measurements. Construct. Build. Mater. 52, 52–58.
Pham, T., Xiao, J.Z., Ding, T., 2015. Simulation study on dynamic response of precast frames made of recycled aggregate concrete. Comput. Concr. 16 (4), 643–667.
Pi, Z.Y., Xiao, H.G., Du, J.J., Liu, M., Li, H., 2019. Interfacial microstructure and bond strength of nano-SiO2-coated steel fibers in cement matrix. Cement Concr. Compos. 103, 1–10.
Pierrehumbert, R., 2019. There is no Plan B for dealing with the climate crisis. Bull. At. Sci. 75 (5), 215–221.
Qian, Y., Kawashima, S., 2018. Distinguishing dynamic and static yield stress of fresh cement mortars through thixotropy. Cement Concr. Compos. 86, 288–296.
Rubio-Hernandez, F.J., Adarve-Castro, A., Velazquez-Navarro, J.F., Paez-Flor, N.M., Delgado-Garcia, R., 2020. Influence of water/cement ratio, and type and concentration of chemical additives on the static and dynamic yield stresses of Portland cement paste. Construct. Build. Mater. 235, 10.
Sanchez Berriel, S., Favier, A., Rosa Dominguez, E., Sanchez Machado, I.R., Heierli, U., Scrivener, K., Martirena Hernandez, F., Habert, G., 2016. Assessing the environmental and economic potential of limestone calcined clay cement in Cuba. J. Clean. Prod. 124, 361–369.
Scrivener, K., Martirena, F., Bishnoi, S., Maity, S., 2018. Calcined clay limestone cements (LC3). Cement Concr. Res. 114, 49–56.
Siddique, S., Jang, J.G., Gupta, T., 2021. Developing marble slurry as supplementary cementitious material through calcination: strength and microstructure study. Construct. Build. Mater. 293.
Snoeck, D., Velasco, L.F., Mignon, A., Van Vlierberghe, S., Dubruel, P., Lodewyckx, P., De Belie, N., 2015. The effects of superabsorbent polymers on the microstructure of cementitious materials studied by means of sorption experiments. Cement Concr. Res. 77, 26–35.
Song, Q.L., Yu, R., Shui, Z.H., Wang, X.P., Rao, S.D., Lin, Z.W., Wang, Z., 2018. Key parameters in optimizing fibres orientation and distribution for ultra-high performance fibre reinforced concrete (UHPFRC). Construct. Build. Mater. 188, 17–27.
Teng, L., Meng, W.N., Khayat, K.H., 2020. Rheology control of ultra-high-performance concrete made with different fiber contents. Cement Concr. Res. 138.
Tosun-Felekoglu, K., Felekoglu, B., Ranade, R., Lee, B.Y., Li, V.C., 2014. The role of flaw size and fiber distribution on tensile ductility of PVA-ECC. Compos. B Eng. 56, 536–545.
Van den Heede, P., De Belie, N., 2012. Environmental impact and life cycle assessment (LCA) of traditional and 'green' concretes: literature review and theoretical calculations. Cement Concr. Compos. 34 (4), 431–442.
Wang, H.T., Wang, L.C., 2013. Experimental study on static and dynamic mechanical properties of steel fiber reinforced lightweight aggregate concrete. Construct. Build. Mater. 38, 1146–1151.
Wang, L., Rehman, N.U., Curosu, I., Zhu, Z., Beigh, M.A.B., Liebscher, M., Chen, L., Tsang, D.C.W., Hempel, S., Mechtcherine, V., 2021. On the use of limestone calcined clay cement (LC3) in high-strength strain-hardening cement-based composites (HS-SHCC). Cement Concr. Res. 144.
Wang, R., Gao, X.J., Huang, H.H., Han, G.S., 2017. Influence of rheological properties of cement mortar on steel fiber distribution in UHPC. Construct. Build. Mater. 144, 65–73.
World-Bank, 2012. New Report Examines Risks of 4 Degree Hotter World by End of Century. World Bank Group.
Xue, J., Shinozuka, M., 2013. Rubberized concrete: a green structural material with enhanced energy-dissipation capability. Construct. Build. Mater. 42, 196–204.
Yaragal, S.C., Kumar, B.C., Jitin, C., 2020. Durability studies on ferrochrome slag as coarse aggregate in sustainable alkali activated slag/fly ash based concretes. Sustain. Mater.Technol. 23.
Yu, J., Wu, H.L., Mishra, D.K., Li, G., Leung, C.K.Y., 2021. Compressive strength and environmental impact of sustainable blended cement with high-dosage Limestone and Calcined Clay (LC2). J. Clean. Prod. 278.
Yudiesky Cancio Díaz a, b., Sofia Sánchez Berriel, a., C, U.H., Aurélie, R.F.d., Inocencio, R.S.M.a., D, K.L.S., José Fernando Martirena Hernández, a., B, G.H., 2017. Limestone calcined clay cement as a low-carbon solution to meet expanding cement demand in emerging economies. Dev. Eng. 2, 82–91.
Zamora-Castro, S.A., Salgado-Estrada, R., Sandoval-Herazo, L.C., Melendez-Armenta, R. A., Manzano-Huerta, E., Yelmi-Carrillo, E., Herrera-May, A.L., 2021. Sustainable development of concrete through aggregates and innovative materials: a review. Appl. Sci.-Basel. 11 (2).
Zhang, H., Wang, B., Xie, A.Y., Qi, Y.Z., 2017. Experimental study on dynamic mechanical properties and constitutive model of basalt fiber reinforced concrete. Construct. Build. Mater. 152, 154–167.
Zhang, W.H., Zeng, W.Z., Zhang, Y.S., Yang, F.H., Wu, P.P., Xu, G.D., Gao, Y.Y., 2020. Investigating the influence of multi-walled carbon nanotubes on the mechanical and damping properties of ultra-high performance concrete. Sci. Eng. Compos. Mater. 27 (1), 433–444.
Zhao, X., Li, Q.H., Xu, S.L., 2020. Contribution of steel fiber on the dynamic tensile properties of hybrid fiber ultra high toughness cementitious composites using Brazilian test. Construct. Build. Mater. 246.
Zhi, Z.Z., Ma, B.G., Tan, H.B., Guo, Y.F., Jin, Z.H., Yu, H.L., Jian, S.W., 2018. Effect of competitive adsorption between polycarboxylate superplasticizer and hydroxypropylmethyl cellulose on rheology of gypsum paste. J. Mater. Civ. Eng. 30 (7).